Article

Shell buckling for programmable metafluids

Adel Djellouli[1,5], Bert Van Raemdonck[2,5], Yang Wang[1,5], Yi Yang[1], Anthony Caillaud[1], David Weitz[1], Shmuel Rubinstein[1,3], Benjamin Gorissen[1,4 ✉] & Katia Bertoldi[1 ✉]

The pursuit of materials with enhanced functionality has led to the emergence of metamaterials—artificially engineered materials whose properties are determined by their structure rather than composition. Traditionally, the building blocks of metamaterials are arranged in fixed positions within a lattice structure[1–19]. However, recent research has revealed the potential of mixing disconnected building blocks in a fluidic medium[20–27]. Inspired by these recent advances, here we show that by mixing highly deformable spherical capsules into an incompressible fluid, we can realize a 'metafluid' with programmable compressibility, optical behaviour and viscosity. First, we experimentally and numerically demonstrate that the buckling of the shells endows the fluid with a highly nonlinear behaviour. Subsequently, we harness this behaviour to develop smart robotic systems, highly tunable logic gates and optical elements with switchable characteristics. Finally, we demonstrate that the collapse of the shells upon buckling leads to a large increase in the suspension viscosity in the laminar regime. As such, the proposed metafluid provides a promising platform for enhancing the functionality of existing fluidic devices by expanding the capabilities of the fluid itself.

Unlike solid metamaterials, metafluids have the unique ability to flow and adapt to the shape of their container without the need for a precise arrangement of their constituent elements. Our goal is to realize a metafluid that not only has these remarkable attributes but also provides a platform for programmable compressibility, optical properties and rheology. To achieve this, we focus on a suspension comprising elastomeric, highly deformable spherical capsules filled with air within an incompressible fluid. We begin by considering centimetre-scale capsules that are fabricated out of silicone rubber (Zhermack Elite Double 32 with initial shear modulus $G = 0.35$ MPa) using 3D-printed moulds[28,29] (see Supplementary Fig. 1 and Supplementary Information for details). As shown in Fig. 1a, we place these capsules in a glass cylindrical container with volume V_{tot} and fill it completely with water. We then load the system by slowly introducing an additional volume ΔV of water via a syringe pump and measure the pressure inside the container with a differential pressure sensor (see also Supplementary Fig. 5).

We start by placing a single capsule with outer radius $R_o = 10$ mm and thickness $t = 2$ mm into a container with $V_{tot} = 300$ ml, leading to an initial capsule volume fraction of $\varphi = 4\pi R_o^3 N/(3V_{tot}) \approx 0.014$ ($N = 1$ denoting the number of capsules in the suspension). We record a pressure–volume curve that is very different from that of water, not only because the capsule makes the fluid more compressible (lowering the initial bulk modulus K_0 to 31 MPa) but also because it introduces a sudden pressure drop at the critical pressure $P = P_{cr}^{up} = 120$ kPa (Supplementary Fig. 1b and Supplementary Video 1). This drop is caused by the snapping of the elastomeric shell and leads to the formation of a dimple, which becomes more accentuated as ΔV is increased (inset in Fig. 1b). When unloading the suspension by decreasing ΔV, the dimple progressively reduces in size and the capsule snaps back to a spherical shape when the pressure passes the critical pressure $P = P_{cr}^{down} = 50$ kPa, leading to a hysteretic response.

To better understand the dependence of the metafluid characteristic on the properties of the capsules, we then consider a larger capsule with $R_o = 30$ mm and $t = 6$ mm in a container with $V_{tot} = 2,850$ ml, so that $t/R_o = 0.2$ remains unaltered and φ increases to 0.04. In this case, the system shows a lower initial bulk modulus ($K_0 = 18$ MPa), but still shows a pressure drop at $P_{cr}^{up} = 120$ kPa (red line in Fig. 1c), suggesting that K_0 and P_{cr}^{up} can be tuned independently by varying φ and t/R_o. Next, we investigate the effect of the number of capsules by placing $N = 27$ capsules with $R_o = 10$ mm and $t = 2$ mm in the same container with $V_{tot} = 2,850$ ml. As both φ and t/R_o remain the same (that is, $\varphi = 0.04$ and $t/R_o = 0.2$), the suspension shows the same initial bulk modulus (green line in Fig. 1c) and all capsules snap at $P \approx P_{cr}^{up}$ (snapshots in Fig. 1c and Supplementary Video 2). However, in this case, the large snapping-induced pressure drop observed for $N = 1$ is replaced by 27 small drops, where each drop corresponds to the collapse of a single capsule. These individual drops occur at roughly the same pressure such that a plateau emerges (see Supplementary Figs. 4–7 for additional experimental results).

The results in Fig. 1a–c are for a fluid containing centimetre-scale capsules, but most applications of fluids require the capability of flowing through small openings. Therefore, we take advantage of microcapillarity[30,31] to fabricate spherical capsules with $R_o \approx 250$ μm and $t \approx 65$ μm out of polydimethylsiloxane (PDMS; Fig. 1d and Supplementary Figs. 2 and 3). We characterize the pressure–volume curve of the resulting microcapsule suspension by placing it in a syringe with volume V_{tot} and slowly displacing the plunger to reduce the enclosed volume by ΔV, while keeping the tip closed and monitoring the pressure (see Supplementary Fig. 10 and Supplementary Information for more details). In Fig. 1e,f, we report the pressure–volume curves measured for a single microcapsule and for a suspension of many microcapsules with $\varphi = 0.3$, respectively (see also Supplementary Videos 1 and 2).

[1]J.A. Paulson School of Engineering and Applied Sciences, Harvard University, Cambridge, MA, USA. [2]Department of Mechanical Engineering, KU Leuven and Flanders Make, Heverlee, Belgium. [3]Present address: The Racah Institute of Physics, The Hebrew University, Jerusalem, Israel. [4]Present address: Department of Mechanical Engineering, KU Leuven and Flanders Make, Heverlee, Belgium. [5]These authors contributed equally: Adel Djellouli, Bert Van Raemdonck, Yang Wang. ✉e-mail: benjamin.gorissen@kuleuven.be; bertoldi@seas.harvard.edu
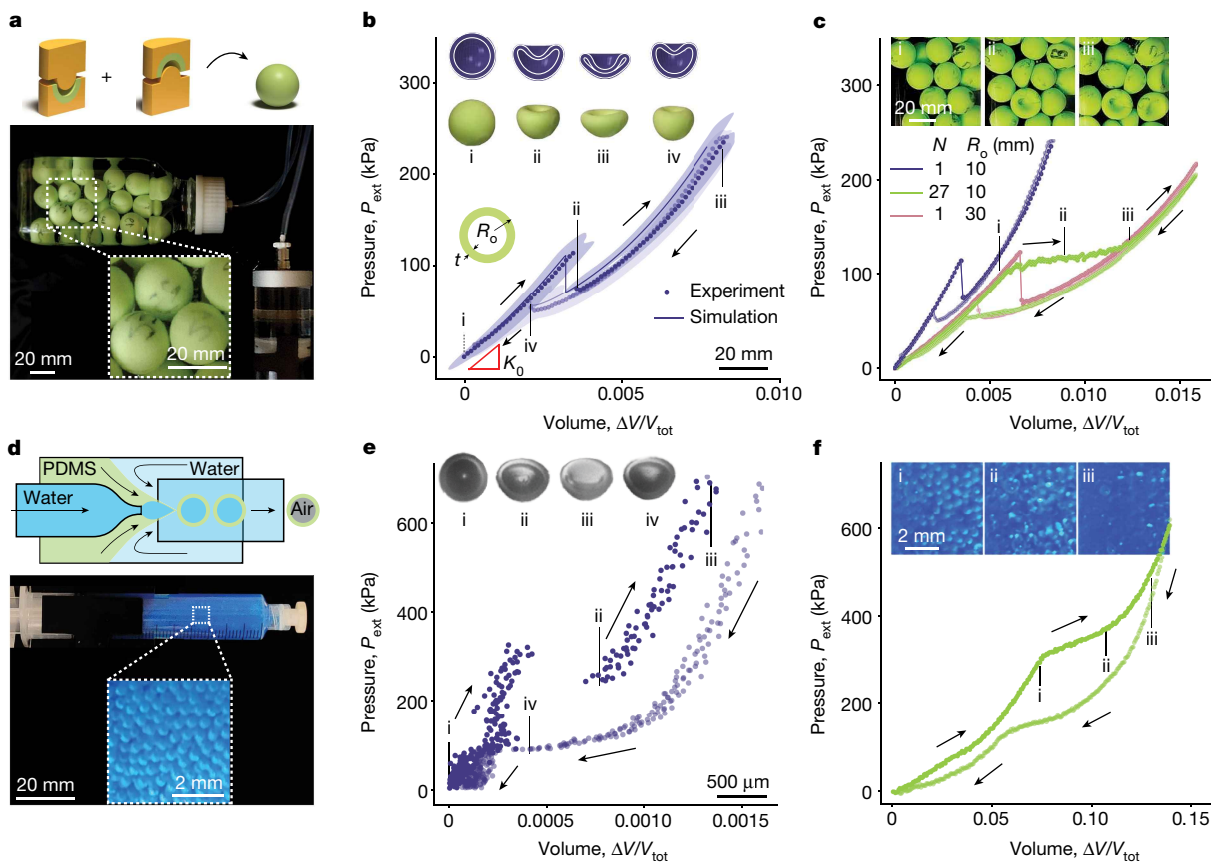
Fig. 1 | Metafluid comprising highly deformable capsules. a, Our centimetre-scale capsules are fabricated via a moulding approach and suspended in a fluid. The resulting metafluid is then pressurized. **b**, Pressure–volume curve of a single centimetre-scale capsule with $t = 2$ mm and $R_o = 10$ mm. Loading (dark purple) and unloading (light purple) curves are shown. The experimental data are depicted as average (dots) and standard deviation (shaded area) of five samples fabricated using the same mould and material. The solid line indicates finite-element results. Insets: experimental (bottom) and numerical (top) snapshots of the capsule. **c**, Experimental pressure–volume curves of metafluids comprising centimetre-scale capsules. Insets: snapshots of the metafluid at different level of compression. **d**, Our micrometre-scale capsules are fabricated from double emulsions using a co-axial flow focusing glass microfluidic device. **e**, Experimental pressure–volume curve of a single micrometre-scale capsule with $t \approx 65$ μm and $R_o = 250$ μm. **f**, Experimental pressure–volume curves of metafluids comprising micrometre-scale capsules with a volume fraction $\varphi \approx 0.3$ suspended in silicone oil. Insets: snapshots of the metafluid at different levels of compression.

The curves show qualitatively similar nonlinear behaviours to their centimetre-scale counterparts, confirming that the response of our metafluids is independent of scale. Nevertheless, it is important to highlight that the metafluid incorporating microscale capsules does not show a clear plateau in the pressure–volume curve. This deviation can be attributed to geometric imperfections introduced during the fabrication process, resulting in polydispersity and a wide range of buckling pressures P_{cr}^{up}.

Modelling

To systematically explore the effect of the capsules on the response of the metafluid, we conduct finite-element analyses using the commercial package ABAQUS 2020 Standard. In our simulations, we assume the deformation to be axisymmetric and use an incompressible Neo–Hookean material model with initial shear modulus G to capture the response of the elastomeric material (see Supplementary Figs. 15–25, Supplementary Tables 1 and 2, and Supplementary Information for additional details). We first conduct implicit dynamic simulations to calculate the difference between the external and internal pressure of the shells, ΔP_{shell}, while slowly decreasing and then increasing the volume of their internal cavity by ΔV (purple line in Fig. 2a). Then we use the ideal gas law to obtain the pressure of the gas enclosed in the shell cavity, P_{int}, as a function of ΔV (cyan line in Fig. 2a). Finally, we take advantage of the shell incompressibility to calculate the pressure on the external surface of the capsule, P_{ext}, as

$$P_{ext} = \Delta P_{shell}(\Delta V) + P_{int}(\Delta V). \tag{1}$$

The results reported in Fig. 2a indicate that, since P_{int} increases monotonically with ΔV, the nonlinear response of the metafluid stems from ΔP_{shell}. We also note that P_{ext} does not scale with G, as P_{int} is independent of the shell material (Supplementary Fig. 19). Further, we point out that if the pressure is controlled during the tests, snapping triggers a jump in volume at P_{cr} (dotted lines in Fig. 2a). Finally, we test the relevance of our model by comparing its predictions with the experimental results reported in Fig. 1b as well as to the experimentally measured P_{cr}^{up} and P_{cr}^{down} for a variety of centimetre-scale capsules (Fig. 2b) and find excellent agreement.

Having established a numerical model that accurately captures the response of the individual capsules, we use it to predict the response of suspensions comprising many capsules. Towards this end, we assume that the capsules are suspended in an incompressible fluid and that the pressure is uniform throughout this medium (thereby neglecting the effects of gravity and viscosity). Under these assumptions, the external pressure is the same for all N capsules

$$P_{ext}^{(1)}(\Delta V^{(1)}) = P_{ext}^{(2)}(\Delta V^{(2)}) = \ldots = P_{ext}^{(N)}(\Delta V^{(N)}), \tag{2}$$
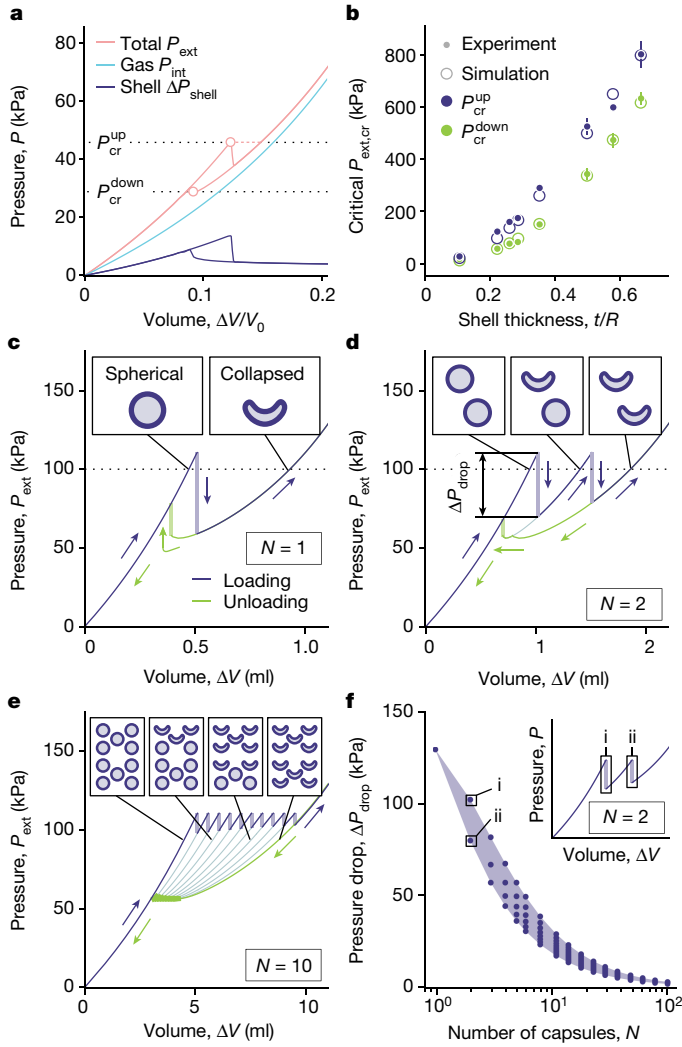
Fig. 2 | Modelling metafluids. a, Numerically predicted pressure–volume curve for a spherical shell with $t/R = 0.22$ and $G = 60$ kPa (cyan line), the gas contained in its internal cavity (blue line) and the resulting capsule (pink line) under volume control. If the capsule is loaded under pressure control, the instabilities are triggered at the circular markers and follow the dotted lines. **b**, Critical pressures as a function of shell thickness for capsules with $G = 350$ kPa. Both numerical (hollow circular markers) and experimental data (dots) are shown. Vertical lines on the experimental data points indicate the standard deviation between shells manufactured with the same mould. **c**–**e**, Numerical pressure–volume curve for a metafluid containing $N = 1$ (**c**), $N = 2$ (**d**) and $N = 10$ (**e**) capsules with $R_o = 10$ mm, $t = 2$ mm and $G = 350$ kPa. Insets: the state of the capsules for different ΔV at $P_{ext} = 100$ kPa. **f**, Evolution of the pressure drop triggered by buckling, ΔP_{drop}, as a function of the number of capsules in a metafluid, N. Inset: the pressure–volume curve for a metafluid comprising $N = 2$ capsules that produces the data points labelled i and ii.

where $\Delta V^{(i)}$ denotes the change in volume of the ith capsule in the pressurized state, which is subjected to the constraint

$$\Delta V = \sum_{i=1}^{N} \Delta V^{(i)}. \tag{3}$$

It is noted that equations (2) and (3) together with the $P_{ext}^{(i)} - \Delta V^{(i)}$ curves extracted from the finite-element simulations are analogous to the relations between force and displacement for chains of bistable elements with trilinear characteristics[32,33], with the only difference being that for the capsules the portion of the pressure–volume curve immediately after snapping is inherently unstable.

Operationally, we determine all of the equilibrium configurations of a metafluid comprising N capsules by first finding all stable $\Delta V^{(i)}$ that result in a predefined set of pressure values for each capsule separately (Fig. 2c). Then for each value of pressure, we construct the possible equilibrium states of the metafluid by making all possible combinations of those volumes. As shown in Fig. 2d,e, for a suspension comprising N identical capsules, this process generates a pressure–volume characteristic with $N + 1$ unique equilibrium branches. When the suspension is loaded by slowly introducing a volume ΔV of incompressible fluid, the first branch is initially followed until the critical buckling pressure of the capsules, P_{cr}^{up}, is reached. At that point, one capsule snaps and the pressure drops (at constant ΔV) until it reaches the next branch. This process then repeats until all N capsules are collapsed, leading to a sawtooth pattern with N peaks at P_{cr}^{up}. As observed in our experiments, we find that the magnitude of the pressure drops that follow the buckling events, ΔP_{drop}, decreases with N (Fig. 2f). This decrease is due to the fact that in a suspension with N capsules, the sudden reduction in volume experienced by one capsule upon snapping can be compensated by a slight expansion of the remaining $N - 1$ capsules (see Supplementary Information for more details). Therefore, for large N, ΔP_{drop} tends to zero and each capsule can be considered to experience pressure control conditions even though the total volume of the metafluid is controlled.

Harnessing the nonlinear metafluid behaviour

Guided by our understanding of the metafluid response, we then harness its highly nonlinear behaviour for functionality. First, we exploit the snapping-induced pressure plateau to realize a gripper that can grasp objects of very different size and compressive strength when actuated with the same input. More specifically, we consider a two-jaw parallel gripper actuated by pressurized fluid (Fig. 3a, top left) and focus on three distinct objects: a glass bottle of 60 mm in diameter and 160 g in weight, an egg of about 25 mm in diameter and about 16 g in weight, and a blueberry of about 10 mm in diameter and about 0.5 g in weight. For a successful grasp, the supplied volume, ΔV, must be large enough for the actuated jaw to reach the object and hold its weight, but not so large as to generate an excessive force that crushes it (Fig. 3a, top right). In particular, for the considered bottle, egg and blueberry, the supplied volume required to reach them and the pressures needed to hold them and crush them are measured as $\Delta V_{reach} \approx 1.1$ ml, $\Delta V_{reach} \approx 3.9$ ml and $\Delta V_{reach} \approx 5.1$ ml, $P_{hold} \approx 110$ kPa, $P_{hold} \approx 12$ kPa and $P_{hold} \approx 1$ kPa, and $P_{crush} \approx 700$ kPa, $P_{crush} \approx 105$ kPa and $P_{crush} \approx 55$ kPa, respectively. When using water or air as fluid to actuate the jaw, no ΔV can be identified that allows us to successfully grasp all three objects (see Supplementary Fig. 8, Supplementary Video 3 and Supplementary Information for more details). By contrast, when using our metafluid with $K_0 = 2$ MPa and two plateaus at 45 kPa and 120 kPa (realized by filling a container with $V_{tot} = 100$ ml with water and six capsules with $t = 2$ mm and $R_o = 10$ mm, three made out of rubber with $G = 60$ kPa and three made out of rubber with $G = 350$ kPa), we can successfully grasp all three objects by injecting $\Delta V = 6.7$ ml (Fig. 3a, bottom, and Supplementary Video 3).

Although in Fig. 3a we use centimetre-scale capsules enclosed in a separate container to regulate the pressure of the fluid, such an independent pressure reservoir is unnecessary when utilizing our microsuspension, as it can be directly placed in the functional components. To demonstrate this, we use the microsuspension of Fig. 1f to directly pressurize a flexible latex tube (shear modulus $G \approx 1$ MPa) with outer diameter of 5.1 mm, thickness of 1.9 mm and length of 48 mm. Such a tube undergoes a ballooning instability at a pressure $P_{cr}^{tube} \approx 400$ kPa, which upon inflation with glycerol is reached for $\Delta V \approx 0.53$ ml (red line in Fig. 3b and Supplementary Video 4). The compliance and pressure plateau of the microsuspension offset the ballooning instability to $\Delta V \approx 0.94$ ml (green line in Fig. 3b and Supplementary Video 4), showing that the nonlinear behaviour of the capsules also provides an
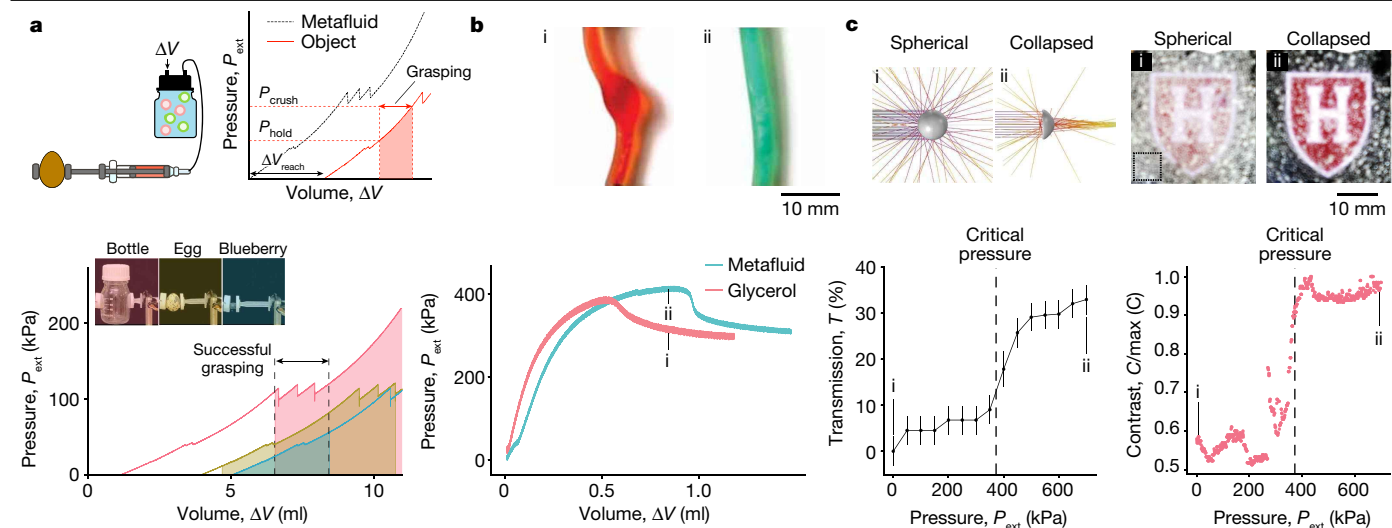
Fig. 3 | Programming metafluids for functionality. a, A two-jaw parallel gripper actuated by our metafluid can grasp a bottle, an egg and a blueberry upon application of the same input $\Delta V = 6.7$ ml (dashed lines in bottom panel). Top left, the experimental setup. Top right, having determined ΔV_{reach}, P_{hold} and P_{crush}, the volume ΔV to be supplied to the system to successfully grasp an object can be easily identified by shifting the pressure–volume curve of the considered fluid (black dashed line) horizontally by ΔV_{reach} for that object. We then identify the volumes ΔV for which $P_{\text{hold}} \leq P_{\text{ext}} \leq P_{\text{crush}}$ (see regions highlighted in red, yellow and blue in the plot). Bottom, the range of ΔV that enables successful grasping of the bottle, egg and blueberry is between the two vertical dashed lines. **b**, Inflation of a flexible tube with our microsuspension. The ballooning instability is delayed to $\Delta V \approx 0.94$ ml. Top, snapshots of the tube upon inflation with glycerol (left) and the metafluid (right) for $\Delta V = 0.9$ ml. Bottom, pressure–volume curves recorded upon inflation with glycerol and the metafluid. **c**, Top left: tunable optics, ray-tracing simulation for spherical and collapsed capsules. Bottom left: relative transmittance T as function of pressure P_{ext}. The black dashed line represents $P_{\text{cr}}^{\text{up}}$ of the metafluid. Top right: a Harvard logo displayed below the metafluid is clearer for $P_{\text{ext}} > P_{\text{cr}}^{\text{up}}$. Bottom right: this is confirmed by the evolution of the contrast C as function of the pressure P_{ext}. The contrast was measured in the region outlined by the dashed square on snapshot (i).

opportunity to tune the interactions of the metafluid with surrounding flexible structures.

Apart from the nonlinear pressure–volume curve, the substantial alterations in the shape of the capsule induced by instability also present opportunities for functionality. Inspired by the configuration-dependent interactions with light observed for droplets[34], we investigate the effect of the pronounced dimple caused by buckling on the optical properties of the metafluid. To this end, we conduct simulations in COMSOL using a ray-tracing algorithm (see Supplementary Information for details). As shown in Fig. 3c, top left, the simulations show that spherical and collapsed capsules show distinct scattering behaviours (Supplementary Figs. 26 and 27). When we then measure the power of the transmitted light through a microsuspension with $\varphi \approx 0.4$ and $P_{\text{cr}}^{\text{up}} \approx 380$ kPa, we find that the transmittance T suddenly increases from $T \approx 8\%$ to $T \approx 30\%$ at $P_{\text{ext}} \approx P_{\text{cr}}^{\text{up}}$ (Fig. 3c, bottom left, and Supplementary Fig. 11). This increase can be attributed to a combination of the lensing effect and the reduction in the coverage area of the capsules in the collapsed state (see Supplementary Figs. 26–28 and Supplementary Information for details). Such a large change in transmittance makes a Harvard logo, positioned beneath the metafluid, much clearer for $P_{\text{ext}} > P_{\text{cr}}^{\text{up}}$ (Fig. 3c, top right, and Supplementary Video 5), as demonstrated by the sharp increase in contrast when the capsules snap (Fig. 3c, bottom right).

The buckling-induced shape change of the capsules also modifies the way in which the metafluid flows. To demonstrate this point, we consider a microsuspension with $\varphi \approx 0.3$ and $P_{\text{cr}}^{\text{up}} = 300$ kPa and investigate its flow in an elliptical channel with major axis $a_{\text{ch}} = 3$ mm and minor axis $b_{\text{ch}} = 750$ μm. We fix the difference of pressure between the inlet and outlet at $\Delta P = P_{\text{in}} - P_{\text{out}} = 50$ kPa and conduct experiments for $P_{\text{in}} \in [50, 450]$ kPa (Fig. 4a, Supplementary Figs. 12 and 13, and Supplementary Video 6). For each experiment, we monitor the position of the front once the flow is fully developed and then calculate its average velocity, $\bar{v}_{\text{front}}$. As expected, we find that for $50 \leq P_{\text{in}} \leq 250$ kPa, the velocity of the front increases with the pressure at the inlet (Fig. 4b). For

this range of P_{in}, the capsules retain their spherical shape and isotropically shrink as the pressure increases, leading to a decreasing effective capsule volume fraction and, in turn, to a faster flow[35–37]. However, when the pressure is high enough to snap the capsules, $\bar{v}_{\text{front}}$ largely decreases. The unexpected drop in flow velocity can be explained by the formation of a dimple upon buckling, which causes the capsules to adopt a concave shape. This concave shape significantly modifies the interactions between particles, resulting in the formation of clusters and aggregates that ultimately slow down the flow[38] (Supplementary Video 6). Importantly, this transition is reversible and repeatable as the shape change of the capsules is driven by an elastic instability (Supplementary Video 6). The results in Fig. 4b suggest that the effective viscosity of the metafluids is higher when the capsules are collapsed. Nonetheless, it is important to note that in these experiments the metafluid is sheared at a rate $\dot{\gamma} \approx 1$ s^{-1}. To investigate how the effective viscosity of the metafluid is affected by the shear rate, we characterize its rheology using a parallel plate rheometer (see Supplementary Fig. 14 and Supplementary Information for details). The results reported in Fig. 4c indicate that the collapse of the particles have a profound effect on its rheology. In the presence of spherical capsules, the metafluid behaves as a Newtonian fluid with effective viscosity $\eta \approx 2.2\eta_0$ (η_0 denoting the viscosity of the solvent). However, when the capsules are collapsed, the suspension transforms into a non-Newtonian shear-thinning fluid. In line with the results in Fig. 4a,b, the metafluid containing collapsed capsules shows high effective viscosity at low shear rates. Such behaviour is ascribed to the formation of clusters by the collapsed particles, as previously reported for blood containing sickle-shaped red blood cells[39]. As the shear rate increases, we observe an initial rapid decrease in effective viscosity, which we attribute to the gradual disruption of the clusters. Eventually, at $\dot{\gamma} \approx 10$ s^{-1} the effective viscosity approaches a plateau at $1.3\eta_0$. This plateau can be attributed to the breakdown of particle clusters at such high strain rates. Finally, we note that at high shear rates, the effective viscosity of the metafluid containing collapsed particles is lower than that of the metafluid containing
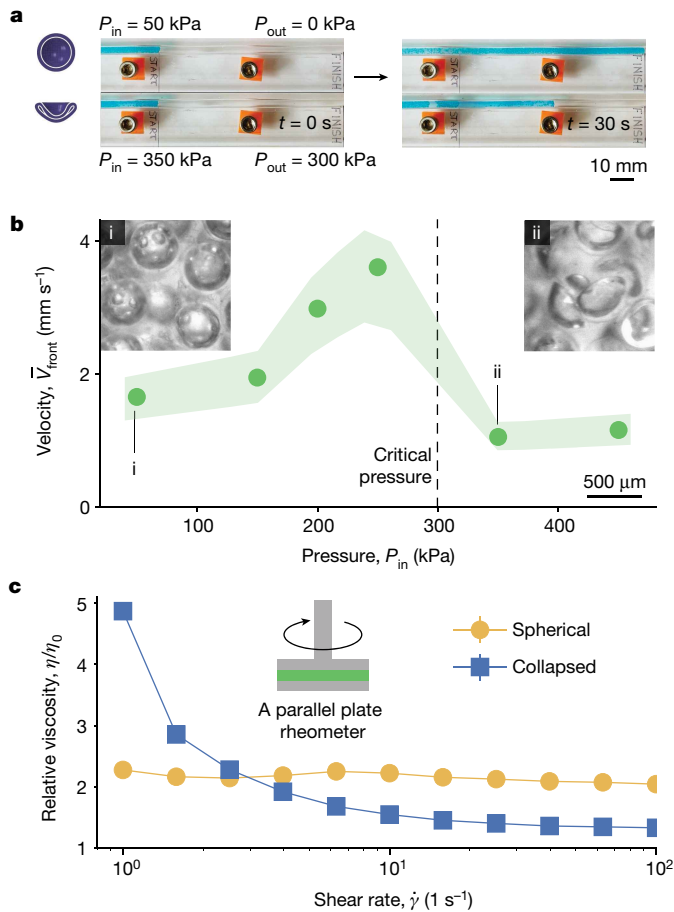
Fig. 4 | Harnessing nonlinearity for tunable rheology. a, Snapshots of the metafluid with $P_{cr}^{up} \approx 300$ kPa flowing in a channel under constant difference of pressure $\Delta P = P_{in} - P_{out} = 50$ kPa at $t = 0$ (left) and $t = 30$ s. Top: $P_{in} = 50$ kPa so that the capsules are spherical. Bottom: $P_{in} = 350$ kPa so that the capsules are collapsed. **b**, Average front velocity as function of P_{in} for $\Delta P = 50$ kPa. The experimental data are depicted as average (markers) and standard deviation (shaded area). Snapshots show the flowing microsuspension for $P_{in} = 50$ kPa and $P_{in} = 350$ kPa. **c**, Flow curves for a metafluid containing spherical (yellow markers) and collapsed (blue markers) capsules.

spherical ones, probably because of the decrease in particle volume fraction caused by buckling. Altogether, these experiments highlight that the metafluid shows rich rheology that can be tuned by controlling shape of the capsules through the level of the applied pressure.

Conclusion

In summary, we have successfully demonstrated the potential of utilizing reversible buckling of elastomeric shells to create a novel class of metafluids. These metafluids show programmable compressibility, switchable optical properties and adjustable viscosity. The versatility of these metafluids opens numerous opportunities for functionality, as demonstrated by the development of adaptable grippers and reconfigurable logic gates (see Supplementary Fig. 9 and Supplementary Information for details). Moreover, we anticipate that the programmability of these metafluids will have significant implications for acoustic and thermodynamic properties, enabling the enhancement of thermodynamic cycles and customizable sound propagation. All these applications would benefit from an inverse design platform capable of identifying shell mixtures that yield desired responses. For example, inversely designed metafluids with complex nonlinear behaviour could be used to modify the functionality of soft actuators by simply changing the actuating fluid instead of redesigning the actuator itself for the new task. Furthermore, they could pave the way towards smart hydraulic shock absorbers with dissipation tailored to the profile of the shock. Finally, while this study primarily focused on situations involving slow loading, dynamic pressure drops across the metafluid could open opportunities for a spatial avalanche of snapping events and interesting wave propagation.

Online content

Any methods, additional references, Nature Portfolio reporting summaries, source data, extended data, supplementary information, acknowledgements, peer review information; details of author contributions and competing interests; and statements of data and code availability are available at https://doi.org/10.1038/s41586-024-07163-z.

1. Engheta, N. & Ziolkowski, R. W. *Metamaterials: Physics and Engineering Explorations* (Wiley, 2006).
2. Craster, R. V. & Guenneau, S. *Acoustic Metamaterials: Negative Refraction, Imaging, Lensing and Cloaking* Vol. 166 (Springer Science & Business Media, 2012).
3. Deymier, P. A. *Acoustic Metamaterials and Phononic Crystals* Vol. 173 (Springer Science & Business Media, 2013).
4. Maldovan, M. Narrow low-frequency spectrum and heat management by thermocrystals. *Phys. Rev. Lett.* **110**, 025902 (2013).
5. Bertoldi, K., Vitelli, V., Christensen, J. & Van Hecke, M. L. Flexible mechanical metamaterials. *Nat. Rev. Mater.* **2**, 17066 (2017).
6. Kadic, M., Bückmann, T., Schittny, R. & Wegener, M. Metamaterials beyond electromagnetism. *Rep. Prog. Phys.* **76**, 126501 (2013). ISSN 0034-4885.
7. Christensen, J., Kadic, M., Kraft, O. & Wegener, M. Vibrant times for mechanical metamaterials (book review). *MRS Commun.* **5**, 453–462 (2015).
8. Lee, G. et al. Piezoelectric energy harvesting using mechanical metamaterials and phononic crystals. *Commun. Phys.* **5**, 94 (2022).
9. Xu, X. et al. Multifunctional metamaterials for energy harvesting and vibration control. *Adv. Funct. Mater.* **32**, 2107896 (2022).
10. Hu, G., Tang, L., Liang, J., Lan, C. & Das, R. Acoustic-elastic metamaterials and phononic crystals for energy harvesting: a review. *Smart Mater. Struct.* **30**, 085025 (2021).
11. Chen, Z., Guo, B., Yang, Y. & Cheng, C. Metamaterials-based enhanced energy harvesting: a review. *Physica B* **438**, 1–8 (2014).
12. Fowler, C., Silva, S., Thapa, G. & Zhou, J. High efficiency ambient RF energy harvesting by a metamaterial perfect absorber. *Opt. Mater. Express* **12**, 1242–1250 (2022).
13. Ramahi, O. M., Almoneef, T. S., AlShareef, M. & Boybay, M. S. Metamaterial particles for electromagnetic energy harvesting. *Appl. Phys. Lett.* **101**, 173903 (2012).
14. Lin, Keng-Te., Lin, H., Yang, T. & Jia, B. Structured graphene metamaterial selective absorbers for high efficiency and omnidirectional solar thermal energy conversion. *Nat. Commun.* **11**, 1389 (2020).
15. Cortés, E. et al. Optical metasurfaces for energy conversion. *Chem. Rev.* **122**, 15082–15176 (2022).
16. Patel, S. K., Surve, J., Katkar, V. & Parmar, J. Optimization of metamaterial-based solar energy absorber for enhancing solar thermal energy conversion using artificial intelligence. *Adva. Theory Simul.* **5**, 2200139 (2022).
17. Chen, T., Li, S. & Sun, H. Metamaterials application in sensing. *Sensors* **12**, 2742–2765 (2012).
18. Molerón, M. & Daraio, C. Acoustic metamaterial for subwavelength edge detection. *Nat. Commun.* **6**, 8037 (2015).
19. Fan, W., Yan, B., Wang, Z. & Wu, L. Three-dimensional all-dielectric metamaterial solid immersion lens for subwavelength imaging at visible frequencies. *Sci. Adv.* **2**, e1600901 (2016).
20. Urzhumov, Y. A. et al. Plasmonic nanoclusters: a path towards negative-index metafluids. *Opt. Express* **15**, 14129–14145 (2007).
21. Sheikholeslami, S. N., Alaeian, H., Koh, Ai. Leen. & Dionne, J. A. A metafluid exhibiting strong optical magnetism. *Nano Lett.* **13**, 4137–4141 (2013).
22. Yang, J. et al. Broadband absorbing exciton-plasmon metafluids with narrow transparency windows. *Nano Lett.* **16**, 1472–1477 (2016).
23. Hinamoto, T., Hotta, S., Sugimoto, H. & Fujii, M. Colloidal solutions of silicon nanospheres toward all-dielectric optical metafluids. *Nano Lett.* **20**, 7737–7743 (2020).
24. Kim, K., Yoo, SeokJae, Huh, Ji-Hyeok, Park, Q.-Han & Lee, S. Limitations and opportunities for optical metafluids to achieve an unnatural refractive index. *ACS Photon.* **4**, 2298–2311 (2017).
25. Cho, Y. et al. Using highly uniform and smooth selenium colloids as low-loss magnetodielectric building blocks of optical metafluids. *Opt. Express* **25**, 13822–13833 (2017).
26. Brunet, T. et al. Soft 3D acoustic metamaterial with negative index. *Nat. Mater.* **14**, 384–388 (2015).
27. Peretz, O., Ben Abu, E., Zigelman, A., Givli, S. & Gat, A. D. A metafluid with multistable density and internal energy states. *Nat. Commun.* **13**, 1810 (2022).
28. Djellouli, A., Marmottant, P., Djeridi, H., Quilliet, C. & Coupier, G. Buckling instability causes inertial thrust for spherical swimmers at all scales. *Phys. Rev. Lett.* **119**, 224501 (2017).
29. Jambon-Puillet, E., Jones, T. J. & Brun, P.-T. Deformation and bursting of elastic capsules impacting a rigid wall. *Nat. Phys.* **16**, 585–589 (2020).
30. Utada, A. S. Monodisperse double emulsions generated from a microcapillary device. *Science* **308**, 537–541 (2005).

Article

31. Chen, Q. Robust fabrication of ultra-soft tunable PDMS microcapsules as a biomimetic model for red blood cells. *Soft Matter* **19**, 5249–5261 (2023).
32. Puglisi, G. & Truskinovsky, L. Mechanics of a discrete chain with bi-stable elements. *J. Mech. Phys. Solids* **48**, 1–27 (2000).
33. Benichou, I. & Givli, S. Structures undergoing discrete phase transformation. *J. Mech. Phys. Solids* **61**, 94–113 (2013).
34. Nagelberg, S. et al. Reconfigurable and responsive droplet-based compound micro-lenses. *Nat. Commun.* **8**, 14673 (2017).
35. Guazzelli, É., Morris, J. F. & Pic, S. *A Physical Introduction to Suspension Dynamics* Cambridge Texts in Applied Mathematics (Cambridge Univ. Press, 2011).
36. Shewan, H. M. & Stokes, J. R. Viscosity of soft spherical micro-hydrogel suspensions. *J. Colloid Interface Sci.* **442**, 75–81 (2015).
37. Shewan, H. M. & Stokes, J. R. Analytically predicting the viscosity of hard sphere suspensions from the particle size distribution. *J. Nonnewton. Fluid Mech.* **222**, 72–81 (2015).
38. Dressaire, E. & Sauret, A. Clogging of microfluidic systems. *Soft Matter* **13**, 37–48 (2017).
39. Chien, S., Usami, S. & Bertles, J. F. Abnormal rheology of oxygenated blood in sickle cell anemia. *J. Clin. Invest.* **49**, 623–634 (1970).

Methods

The details of the fabrication methods are summarized in Supplementary Information section 1. The experimental procedure for all the experiments conducted for this study are described in Supplementary Information section 2. Finally, information about the modelling is provided in Supplementary Information section 3.

Data availability

The data that support the findings of this study are openly available in GitHub at https://github.com/BertVanRaemdonck/Buckling-Capsule-Metafluids.

Author contributions A.D., B.G., B.V.R. and K.B. proposed and developed the research idea. A.D., Y.Y. and A.C. designed and fabricated the centimetre-scale capsules. Y.W. fabricated and characterized the micrometre-scale capsules. A.D. designed and conducted the experiments and optical simulations. B.V.R. conducted the numerical calculations. A.D., B.V.R. and K.B. wrote the paper. K.B., B.G., S.R. and D.W. supervised the research.

Competing interests The authors declare no competing interests.

Additional information

Supplementary information The online version contains supplementary material available at https://doi.org/10.1038/s41586-024-07163-z.

Correspondence and requests for materials should be addressed to Benjamin Gorissen or Katia Bertoldi.

Peer review information *Nature* thanks Thomas Brunet, Corentin Coulais and the other, anonymous, reviewer(s) for their contribution to the peer review of this work. Peer reviewer reports are available.

Reprints and permissions information is available at http://www.nature.com/reprints.